



IR-Driven strong plasmonic-coupling on Ag nanorices/W₁₈O₄₉ nanowires heterostructures for photo/thermal synergistic enhancement of H₂ evolution from ammonia borane



Yang Liu^a, Zhenyi Zhang^{a,*}, Yurui Fang^b, Benkang Liu^a, Jindou Huang^a, Fujun Miao^c, Yanan Bao^a, Bin Dong^{a,*}

^a Key Laboratory of New Energy and Rare Earth Resource Utilization of State Ethnic Affairs Commission, Key Laboratory of Photosensitive Materials & Devices of Liaoning Province, School of Physics and Materials Engineering, Dalian Nationalities University, 18 Liaohe West Road, Dalian, 116600, PR China

^b Key Laboratory of Materials Modification by Laser Electron, and Ion Beams (Ministry of Education), School of Physics, Dalian University of Technology, Dalian, 116024, PR China

^c School of Materials Science and Engineering, Zhengzhou University, 100 Kexue Avenue, Zhengzhou, 45001, PR China

ARTICLE INFO

Keywords:

Plasmonic coupling
Photo/thermal catalysis
H₂ evolution
W₁₈O₄₉ nanowires
Ag nanorices

ABSTRACT

Plasmonic coupling between two or more metal nanostructures has attracted significant interest, since this fascinating near-field interaction is more effective for the aggregation/magnification of the incident light intensity compared to normal surface-plasmon-resonance (SPR) of single nanostructures. Herein, we report, for the first time, an IR-driven strong plasmonic coupling in an unusual metal/non-metal heterostructure system. This system is fabricated through random assemblage of Ag nanorices (NRs) onto W₁₈O₄₉ nanowires (NWs) film with F-doped SnO₂ glass as substrate. Through the 3D-finite element simulation, we demonstrate that the plasmonic coupling between Ag NRs and W₁₈O₄₉ NWs significantly enhances the localized electric fields at the “hot spots”. This achieved magnitudes of 10¹–10⁴ times of that of incident light, thus leading to the promoted generation of plasmonic “hot-electrons”. Moreover, the resonance excitation of plasmonic coupling on the heterostructures not only induces ultrafast electron transfer from W₁₈O₄₉ to Ag hetero-components, but also the photothermal effect to increase the localized temperature. Upon SPR-coupling excitation, the Ag/W₁₈O₄₉ heterostructures film exhibits a remarkable enhancement of the photo/thermal catalytic activity for H₂ evolution from ammonia borane compared to that of either the Ag NRs (~8.2 ×) or W₁₈O₄₉ NWs (~9.0 ×) films. Notably, we observed an obvious H₂ evolution over the Ag/W₁₈O₄₉ heterostructures film under natural sunlight irradiation.

1. Introduction

The excessive consumption of non-sustainable fossil fuels intensifies air pollution and energy shortage. Formulating an economical and environmental-friendly strategy to convert solar energy into preservable chemical fuels is therefore a matter of utmost urgency. Photocatalytic hydrogen (H₂) evolution either through water splitting or hydrogen-carrier molecules reduction is a promising method toward achieving clean and renewable energy [1–8]. Although there has been much progress in this research field, the efficiency of traditional semiconductor photocatalysts is still unsatisfactory. Two critical obstacles on these photocatalysts are the poor light absorption in low-energy photons and the fast recombination of photogenerated electron-hole pairs [9]. Recently, many attempt to address the above two issues have focused on the construction of noble metal/semiconductor

heterostructures [10,11]. These enhance the photon absorption and utilization in visible-infrared (IR) region based on the surface plasmon resonance (SPR) of noble metals by means of plasmonic “hot electron” injection [12–17]. However, the thus achieved plasmon-driven photocatalytic efficiency is extremely low due to the high potential barrier that limits the hot-electron transfer at the heterostructure interface. Current research indicates that the single noble-metal nanostructure alone is also capable to drive the photocatalytic H₂ evolution from several hydrogen-carrier molecules [18–21]. Upon resonance excitation, the plasmon-generated hot-electron on the surface of noble metal nanostructures can directly transfer to the hydrogen-carrier molecules for H₂ evolution, thus leading to an improved photocatalytic activity compared to noble metal/semiconductor heterostructures [16,22]. However, both the generation and transfer processes of plasmonic hot electrons are inhibited by ultrafast electron-phonon relaxation in the

* Corresponding author.

E-mail addresses: zhangzy@dlnu.edu.cn (Z. Zhang), dong@dlnu.edu.cn (B. Dong).

noble metal nanostructures, which severely weakens the SPR-catalytic activities. In a plasmonic point of view, the SPR-coupling effect between two or more noble metal nanostructures can greatly enhance the localized electromagnetic field and thus strongly boost the generation of hot electrons toward the photocatalytic reaction [23–25]. Currently, the high-cost of noble metals restricts large-scale practical applications. Therefore, it is necessary to find an economical and available plasmonic non-metal material to replace the role of noble metals in the SPR-coupling process.

Recently, the SPR phenomenon has also been observed in several non-metal nanostructures of heavily-doped semiconductors, such as Cu_{2-x}S, Sn-doped In₂O₃, WO_{3-x}, and MoO_{3-x} [26–34]. Unlike the widely investigated noble metals, the SPR in non-metallic semiconductor nanostructures originates from the collective oscillations of excessive free carriers that are associated with ion doping or lattice vacancies. This results in a broad and robust IR-light absorption. In particular, blue W₁₈O₄₉, which is a type of nonstoichiometric tungsten oxide, shows an intense SPR absorption in both the visible and IR region due to abundant oxygen vacancies on its surface [35]. Such a fascinating optical feature suggests plasmonic W₁₈O₄₉ nanostructures as potential substitutes to be coupled with noble metal nanostructure, thus enabling highly efficient plasmonic hot-electron generation and transfer processes. This avoids the disadvantages associated with traditional noble metals SPR-coupling systems. Interestingly, several research groups have reported SPR-enhanced catalytic activities over plasmonic W₁₈O₄₉ nanostructures through plasmonic “hot electron” and the localized photothermal effect under irradiation with IR-light [35–38]. Moreover, the photo/thermal synergistic catalysis combining photochemical and thermochemical conversion has appeared as a promising method for improving catalytic activities, owing to the solar thermal technologies and plasmonic resonance effects [39–44]. However, to date, research of IR-induced strong plasmonic-coupling in metal/non-metal heterostructures has been rarely reported and the corresponding photocatalysis mechanism for the H₂ evolution remains unclear (Scheme 1).

In this work, we develop a novel type of plasmonic coupling heterostructures film through assembling Ag nanorices (NRs) onto W₁₈O₄₉

nanowires (NWs) that are solvothermally grown on a F-doped SnO₂ (FTO) glass surface. By combining the 3D-finite element method (3D-FEM) simulation with surface temperature imaging, we demonstrate that the IR-excitation of plasmonic coupling between Ag NRs and W₁₈O₄₉ NWs can not only induce a 10¹–10⁴ fold enhancement of localized electric fields at the plasmonic “hot spots”, but it can also increase the localized temperature up to ~99°C based on the photothermal effect. Further investigation using the transient absorption (TA) spectroscopy indicates that an ultrafast transfer of photoinduced electron from the W₁₈O₄₉ to Ag hetero-components occurs in their heterostructures, which effectively hinders “hot electron” relaxation. Thus, upon IR-light irradiation, a plasmonic-coupling-enhanced photo/thermal-catalytic H₂ evolution from ammonia borane (NH₃BH₃) over the Ag/W₁₈O₄₉ heterostructures film was observed. Importantly, when focused natural sunlight was used to initiate plasmonic catalysis, the H₂-evolution rate of the Ag/W₁₈O₄₉ heterostructure film could reach ~2.76 μmol h⁻¹.

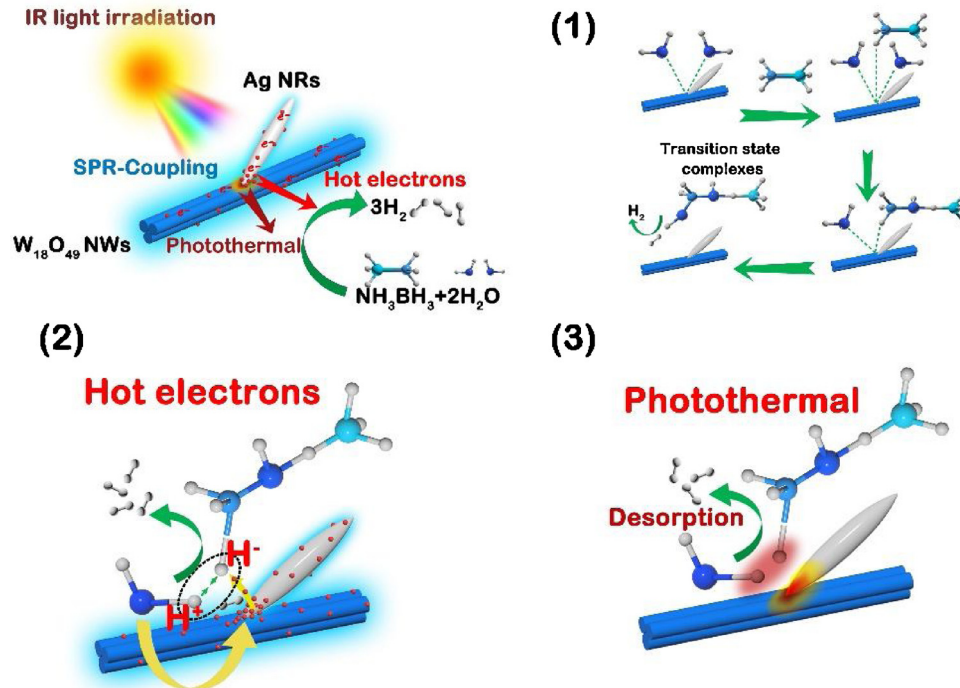
2. Experimental

2.1. Materials

Polyvinyl pyrrolidone (PVP K-30), silver nitrate (AgNO₃), polyethylene glycol 600 (PEG 600), hexacarbonyl tungsten (W(CO)₆), absolute ethanol, were purchased and used without purification.

2.2. Synthesis of silver nanorices (Ag NRs)

2.1 mL of polyvinyl pyrrolidone (PVP K-30) (1 M) and 0.3 mL of aqueous solution of AgNO₃ (1 M) were added into 15 mL of polyethylene glycol 600 (PEG 600) in a 100 mL flask. The flask was transferred to an oil bath at a temperature of 113 °C. The resulting solution was stirred at 113 °C for 8 h. Then, the flask was immediately removed from the oil bath, thus obtaining gray silver colloids. The Ag NRs can be separated from solution after adding a large amount of ethanol, followed by centrifugation at 9000 rpm for 15 min. 4–6 circles were



Scheme 1. Schematic diagram of the photo/thermal catalysis of ammonia borane for H₂ evolution over the Ag/W₁₈O₄₉ heterostructure with plasmonic-coupling effect upon resonance excitation.

repeated. Finally, the precipitates of Ag NRs were re-dispersed in 5 mL of ethanol for use in the following experiment.

2.3. Synthesis of plasmonic $W_{18}O_{49}$ nanowires (NWs) film on FTO glass

In a typical process, 25 mg of $W(CO)_6$ was dissolved into 20 mL of absolute ethanol with constant stirring to form a yellow transparent solution. Then, a cleaned F-doped SnO_2 (FTO) glass with size of 2 cm × 3 cm was placed into a Teflon-lined autoclave loaded with the above solution. The autoclave was sealed and then maintained at 180 °C for 12 h. The obtained sample on the FTO glass with blue color was removed from the reaction solution, washed with ethanol, and finally dried in nitrogen.

2.4. Fabrication of plasmonic-coupling $Ag/W_{18}O_{49}$ heterostructure films

The $Ag/W_{18}O_{49}$ heterostructures film was obtained by assembling Ag NRs onto $W_{18}O_{49}$ NWs surface through a solvent evaporation method combined with a photoreduction process. In this process, 1 mL of Ag NRs (0.06 M) -dispersed ethanol solution was dropped into 10 mL of deionized water and ethanol solution (v:v 1:1) ultrasonic treatment for 15 min. After that the FTO glass loaded with plasmonic $W_{18}O_{49}$ NWs film was immersed vertically into the above solution and put in an oven at 40 °C for 3 h. With a slow evaporation of the mixed solvent, the $Ag/W_{18}O_{49}$ heterostructures film was formed preliminarily. Finally, the product was placed in an ethanol solvent and irradiated at IR light for 5 min to form the plasmonic-coupling $Ag/W_{18}O_{49}$ heterostructures film.

By using the same method, the control samples of the Ag NRs-loaded FTO film and the $Ag/W_{18}O_{49}$ heterostructure films with different amounts of Ag NRs (0.015 mmol, 0.03 mmol, 0.09 mmol) were also fabricated to further investigate the effect of plasmonic coupling resonance on the performance of catalyst property. In the following discussion, the different amounts of Ag NRs (0.015 mmol, 0.03 mmol, 0.06 mmol and 0.09 mmol) loaded on $W_{18}O_{49}$ NWs film were denoted as (1) Ag (0.015)/ $W_{18}O_{49}$ NWs heterostructures film, (2) Ag (0.03)/ $W_{18}O_{49}$ NWs heterostructures film, (3) Ag (0.06)/ $W_{18}O_{49}$ NWs heterostructures film, and (4) Ag (0.09)/ $W_{18}O_{49}$ NWs heterostructures film, respectively.

2.5. Characterization

X-ray diffraction (XRD) patterns of the as-synthesized samples were recorded by a Shimadzu XRD-6000 X-ray diffractometer with a $Cu K\alpha$ line of 0.1541 nm. Scanning electron microscopy (Field Emission-SEM; Hitachi-S4800) and transmission electron microscopy (TEM; JEOL JEM-2100) were used to observe the morphologies and structures of the samples. X-ray photoelectron spectroscopy (XPS) was performed on a VG-ESCALAB LKII instrument with a $Mg K\alpha$ ADES ($h\nu = 1253.6$ eV) source at a residual gas pressure below 10^{-8} Pa. The UV-vis-NIR absorption spectra of the samples were recorded on a Lambda 750 UV-vis-NIR spectrophotometer (Perkin-Elmer, USA).

2.6. Finite element method (FEM) simulation

All full wave numerical simulations were performed with the 3D-finite element method (3D-FEM, commercial software package, Comsol Multiphysics 5.0). The $W_{18}O_{49}$ (permittivity was obtained with the following simulation) nanowire (diameter $D_1 = 10$ nm, length $L = 800$ nm) bundle (three wires touching each other) was placed in a homogeneous surrounding medium with an effective refractive index of 1.0. Ag NR (diameter $D_2 = 100$ nm, length $L = 500$ nm) was put in direct contact with the $W_{18}O_{49}$ NW at different positions.

2.7. Catalytic H_2 evolution upon IR light excitation

The as-synthesized catalysts loaded on the FTO glasses were placed

vertically into a photoreactor with the volume of 35 mL. Then, 10 mL of deionized water was added in a photoreactor above mentioned. The reactor was sealed and degassed by argon for 10 min. Subsequently, 2 mL of deionized water containing 2 mg of NH_3BH_3 was injected into the photoreactor that was exposed under a 300-W Xe lamp (PL-SXE300UV) coupled with IR light filters ($\lambda > 750$ nm) with light density of $5.4\text{ mW}\cdot\text{cm}^{-2}$. The generated H_2 was periodically analyzed by a gas chromatograph (GC) equipped with a thermal conductivity detector (TCD) (Beifen - Ruili Analytical Instrument, SP-3420 A). The catalytic reaction temperatures were kept through placing the quartz reactor into a sink connected with the reflux water condenser.

2.8. Catalytic H_2 evolution upon focused sunlight irradiation

The as-synthesized catalysts loaded on the FTO glasses were placed vertically into a photoreactor with the volume of 35 mL. Then, 10 mL of deionized water was added in a photoreactor above mentioned. The reactor was sealed and degassed by argon for 10 min. Subsequently, 2 mL of deionized water containing 2 mg of NH_3BH_3 was injected into the photoreactor that was exposed under the natural sunlight (with light density of $550\text{ mW}\cdot\text{cm}^{-2}$) irradiation for 1 h. The generated H_2 was periodically analyzed by a gas chromatograph (GC) equipped with a thermal conductivity detector (TCD) (Beifen-Ruili Analytical Instrument, SP-3420 A).

2.9. Apparent quantum efficiency measurement

The apparent quantum efficiency (QE) was measured at 1250 nm by using a 300 W Xe lamp (PLS-SXE300UV) coupled with a monochromator under the identical reaction condition for H_2 production. The number of incident photons from the 300 W Xe lamp is measured with a power meter (70260, Newport Corp.). The QE value can be calculated by using the following equation:

$$AQE = \frac{2 \times \text{number of evolved hydrogen molecules}}{\text{number of incident photons}} \times 100\%$$

2.10. Photoelectrochemical measurement

The photocurrent responses were performed using an electrochemical analyzer (CHI 660D, CH Instruments Inc.) in a standard three-electrode configuration. Pt wire and $Ag/AgCl$ were employed as the counter and reference electrode, respectively. The samples loaded on the FTO glasses with an effective area of 2 cm × 1 cm were prepared as the working electrode. Before irradiation, the HCl aqueous solution (0.2 M) was used as the electrolyte solution. Then, the as-prepared working electrode was irradiated under a 300-W Xe lamp (NBET, HSX-F300) coupled with a monochromator (NBET) to modulate the wavelength of the incident light.

2.11. Ultrafast transient absorption spectroscopy measurement

The femtosecond transient absorption measurements were performed based on a 1 kHz Ti:Sapphire Coherent Astrella regenerative amplifier from Coherent (6 mJ/pulse, 35 fs (fwhm) at 400 nm) combined with Helios transient absorption spectrometer (Ultrafast Systems). Briefly, the fundamental output beam was split in two parts with a 50% beam splitter. The transmitted part was directed into a TOPAS Optical Parametric Amplifier (OPA) to generate tunable excitation (250 nm ~ 2.5 μm) as pump beam. The other part less than 10% was used to generate a white light continuum which was used for probe beam. The pump and probed beam were focused and overlapped into a spot on the solution. Solution was carried in a 2-mm pathlength quartz cuvettes and was stirred continuously throughout the whole experiment. All transient spectra and kinetics were obtained by averaging at least five scans and performed at room temperature.

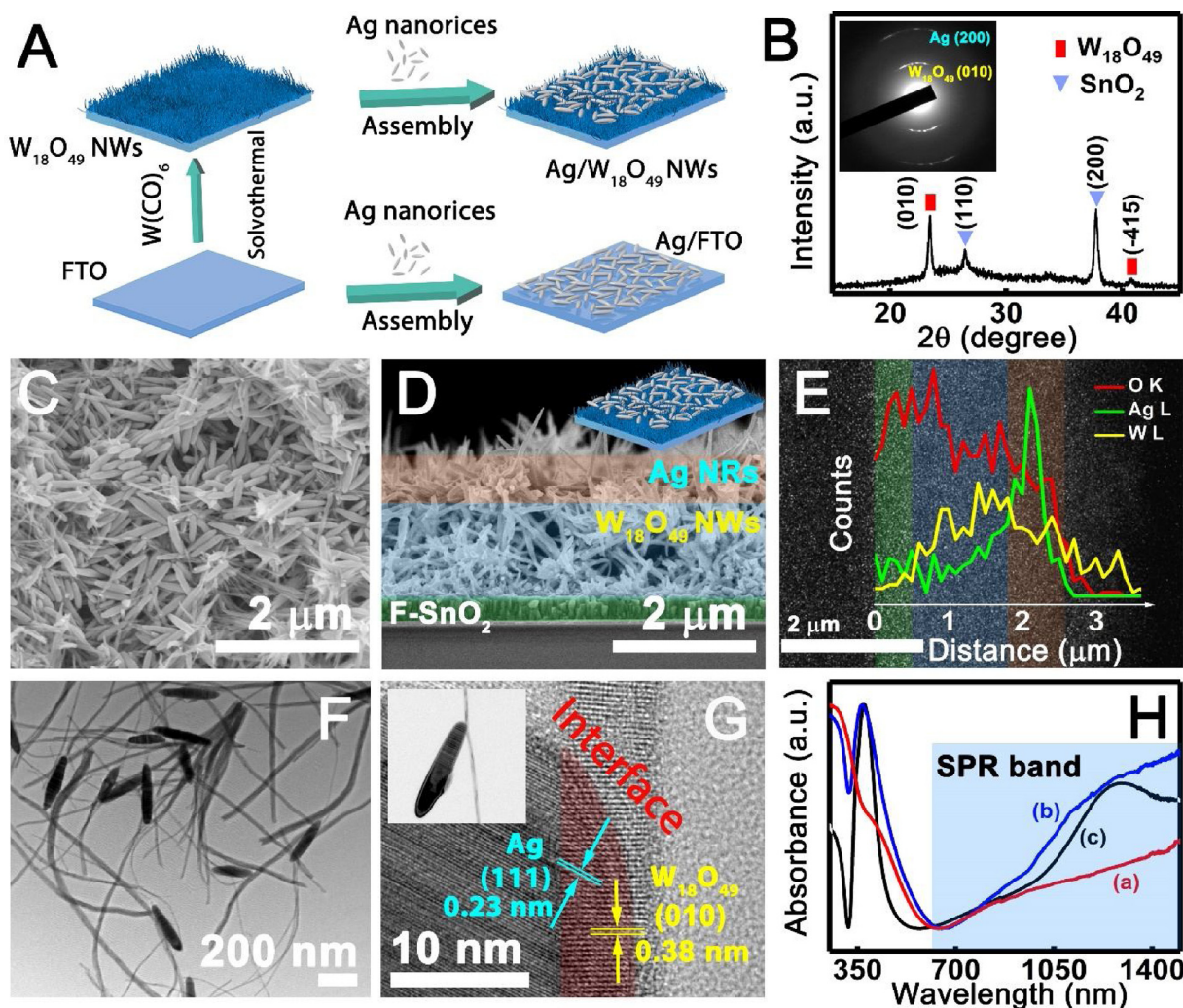


Fig. 1. (A) Fabrication processes of the Ag NRs, W₁₈O₄₉ NWs, and Ag/W₁₈O₄₉ heterostructure films. (B) XRD pattern of the Ag/W₁₈O₄₉ heterostructure film; inset shows the SAED pattern of the Ag/W₁₈O₄₉ heterostructures; SEM images of (C) top view and (D) cross view of the Ag/W₁₈O₄₉ heterostructure film; (E) The EDX spectrum of the Ag/W₁₈O₄₉ heterostructure film, in which the x axle denotes the depth along the vertical direction of Fig. 1D; (F) TEM image of the Ag/W₁₈O₄₉ heterostructures exfoliated from the FTO substrate. (G) HRTEM image of the Ag/W₁₈O₄₉ hetero-interface; (H) UV-Vis-IR absorption spectra of the as-fabricated films: (a) W₁₈O₄₉ NWs; (b) Ag/W₁₈O₄₉ heterostructures; (c) Ag NRs.

3. Results and discussion

Plasmonic-coupling metal/non-metal films of Ag/W₁₈O₄₉ heterostructures with controllable contents of Ag were fabricated through a facile two-step route (Fig. 1A): (i) slantwise growth of W₁₈O₄₉ NWs onto a F-doped SnO₂ (FTO) glass substrate via solvothermal technique; (ii) random assembly of Ag NRs onto the above W₁₈O₄₉ NW surface to form a plasmonic-coupling heterostructure film through a solvent evaporation method combined with a photoreduction process. Based on the similar fabrication method, a pure Ag NRs film (as the control sample) was also fabricated by directly assembling Ag NRs onto the FTO glass. Fig. 1B shows the X-ray diffraction (XRD) pattern of the Ag/W₁₈O₄₉ heterostructure film. Four diffraction peaks can be seen at 23.5°, 40.7°, 26.5°, and 37.7° that belong to the W₁₈O₄₉ (010), W₁₈O₄₉ (-415), SnO₂ (110), and SnO₂ (200) planes, respectively [W₁₈O₄₉-JCPDS (05-0392) and SnO₂-JCPDS (46-1088)]. Please note that the lack of the diffraction peaks of Ag hetero-component can be ascribed to the low content in the Ag/W₁₈O₄₉ heterostructures film.

Scanning electron microscopy (SEM) images show both the top surface (Fig. 1C) and the cross section (Fig. 1D) of the Ag/W₁₈O₄₉ heterostructure film. These show that the Ag NRs with diameters of 40–80 nm and lengths of 200–400 nm are randomly loaded on the top

surface of W₁₈O₄₉-NWs film. Furthermore, the W₁₈O₄₉ NWs grown on the FTO surface have smaller diameters (20–40 nm), but much longer lengths (0.5–2.0 μm) compared to Ag NRs. The elemental distributions on the corresponding SEM images (Fig. 1E and S1) were obtained through the energy dispersive X-ray (EDX) spectra. The results indicate that the Ag NRs are in direct contact with the W₁₈O₄₉ NWs and form a heterostructure layer with a depth of ~1 μm away from the top surface of the film. Fig. 1F shows the transmission electron microscopy (TEM) image of the heterostructures exfoliated from the FTO substrate, which further confirms that the Ag NRs attached to the W₁₈O₄₉ NWs with different contact types, including tip-on-side with different angles, side-by-side, and cross types. Further observation via high-resolution TEM (HR-TEM) imaging indicates the formation of an intimate hetero-interface between the Ag and W₁₈O₄₉ components in their heterostructures (Fig. 1G). Moreover, the lattice fringes with distances of ~0.23 and ~0.38 nm can be ascribed to the Ag (111) and W₁₈O₄₉ (010) planes, respectively. This suggests that the one-dimensional (1D) nanostructures of Ag and W₁₈O₄₉ grow correspondingly along the [111] and [010] directions. Furthermore, the selected-area electron diffraction (SAED) pattern of the Ag/W₁₈O₄₉ heterostructures displays two sets of diffraction rings, belonging to monoclinic W₁₈O₄₉ (010) and cubic Ag (200), respectively (See inset of Fig. 1B). This implies the

existence of both Ag and $W_{18}O_{49}$ components in the heterostructures film.

Fig. 1H shows the UV-vis-NIR absorption spectrum of the as-fabricated Ag/ $W_{18}O_{49}$ heterostructures film in comparison to pure Ag and $W_{18}O_{49}$ films. Two modes of surface plasmon resonance (SPR) can be seen on the absorption curve of the Ag NRs film, where the absorption bands with peaks at ~400 and ~1250 nm originate from the transversal (T-) and the longitudinal (L-) SPR of the anisotropic Ag NR, respectively [45,46]. Moreover, the $W_{18}O_{49}$ NWs on the FTO glass also show two absorption bands: one peak at ~400 nm could be attributed to the interband absorption of the semiconductor feature, while another peak ranging from 650 nm to IR region could be attributed to the SPR band, arising from the collective oscillations of excess electrons on $W_{18}O_{49}$ surface due to the existence of abundant oxygen vacancies [3]. Interestingly, after assemblage of Ag NRs onto the $W_{18}O_{49}$ NWs to form the Ag/ $W_{18}O_{49}$ heterostructures film, the plasmonic band in the IR region becomes much stronger than that of either the Ag NRs or the $W_{18}O_{49}$ NWs films. Furthermore, the curve profiles of SPR bands from the Ag/ $W_{18}O_{49}$ heterostructure film are distinctly different from the summation curves of the SPR bands between the Ag and $W_{18}O_{49}$ films. These results imply strong plasmonic-coupling between Ag NRs and $W_{18}O_{49}$ NWs in their heterostructure film.

In theory, the SPR coupling effect strongly depends on the sizes, geometries, and positions of the plasmonic components in their heterostructures [24]. To investigate the intensity and distribution of the localized electric-field induced by SPR coupling between Ag NRs and $W_{18}O_{49}$ NWs in their heterostructures film, 3D simulations were performed by using the finite element method (FEM), as shown in Fig. 2B and Fig. S2. Please note that in the presented case, Ag NRs are randomly deposited onto the surface of plasmonic $W_{18}O_{49}$ NWs, resulting in various contact types between Ag NRs and $W_{18}O_{49}$ NWs in their heterostructures film. Here, four typical contact types in the Ag/ $W_{18}O_{49}$ heterostructures were selected according to the TEM images (Fig. 2A). The corresponding heterostructures were simplified as binary heterostructure models, as illustrated in the insets of Fig. 2C, respectively. During the simulation processes, the wavelengths at 1000, 1200, and 1400 nm were used to excite the SPR coupling of the simplified models, since these photon energies locate at the SPR band of Ag/ $W_{18}O_{49}$ heterostructures (See Fig. 1H). Upon resonance excitation to drive the SPR-coupling of Ag/ $W_{18}O_{49}$ heterostructures, all simplified models achieved remarkable enhancements of the localized electric fields at their plasmonic “hot spot” regions near the Ag/ $W_{18}O_{49}$ interface. Moreover, the enhancement factor ($|E|^2/|E_0|^2$) of the electric-field intensity increases with the changing excitation energy from 1000 to 1400 nm (Fig. 2C). This wavelength-dependent enhancement of the electric field intensity matches well with the SPR band of Ag/ $W_{18}O_{49}$ heterostructures. This confirms that the SPR-coupling of the Ag/ $W_{18}O_{49}$ heterostructure can strongly aggregate and amplify the incident IR-photon intensity at their interfaces. When the tip of the Ag NR touches the side surface of a $W_{18}O_{49}$ NW to form the contact types of tip-on-side with the angles of 45° and 90°, the enhancement factors of $|E|^2/|E_0|^2$ reached $\sim 3.58 \times 10^3$ and $\sim 5.15 \times 10^4$, respectively, at the corresponding “hot spot” of Ag/ $W_{18}O_{49}$ interface under 1400-nm excitation. These enhancement factors far exceed the values obtained from the Ag/ $W_{18}O_{49}$ heterostructures with the contact type of either side-by-side ($\sim 1.91 \times 10$) or cross ($\sim 4.00 \times 10^2$) types. In general, the enhanced intensity of the localized electric field dramatically increases the “hot electron” generation and the localized temperature at the plasmonic “hot spot” of the nano-heterostructures interface/surface [47]. Thus, it is reasonable to suggest that strong plasmonic coupling occurs on the Ag/ $W_{18}O_{49}$ heterostructure film under IR-light excitation, which is beneficial for the improvement of both the kinetics process of plasmonic “hot electron” and the photothermal effect towards the photo/thermal synergistic catalytic reaction.

From the viewpoint of a highly efficient utilization of solar energy, the development of IR-driven photo-functional materials is desirable,

because the low-energy infrared radiation comprises ~44% of the incident solar energy [48]. Here, the Ag/ $W_{18}O_{49}$ heterostructure film was employed as a solar-energy conversion device to catalyze the NH_3BH_3 hydrolysis for the releasing of H_2 fuel. At first, we investigated the IR-excited ($\lambda > 750$ nm) catalytic activity of the Ag/ $W_{18}O_{49}$ heterostructure film for H_2 evolution. A control experiment in absence of both the plasmonic heterostructures film and the light irradiation showed no H_2 evolution at room temperature (20°C). Upon IR-light irradiation, the aqueous solution of NH_3BH_3 releases trace amounts of H_2 at a slow rate ($\sim 0.01 \mu\text{mol min}^{-1}$), as shown in Fig. 3A. This indicates an extremely weak hydrolysis of NH_3BH_3 without photocatalyst. The addition of $W_{18}O_{49}$ NWs film into the NH_3BH_3 aqueous solution leads to a slight improvement of the H_2 evolution rate ($\sim 0.02 \mu\text{mol min}^{-1}$), which can be attributed to the IR-induced synergistic effect between the “hot electron” generation and the photothermal effect due to the SPR excitation. Accordingly, the plasmonic Ag NRs film also displays a specific photo-activity for H_2 evolution with a rate of $\sim 0.022 \mu\text{mol min}^{-1}$ after SPR excitation by IR light. Interestingly, after assembling Ag NRs onto the $W_{18}O_{49}$ NWs film, the obtained Ag/ $W_{18}O_{49}$ heterostructures film exhibits a remarkable enhancement of catalytic activity with the H_2 -evolution rate ($\sim 0.18 \mu\text{mol min}^{-1}$) exceeding that of either pure Ag NRs or $W_{18}O_{49}$ NWs films by almost one order of magnitude. Moreover, large numbers of bubbles were observed on the surface of the Ag/ $W_{18}O_{49}$ heterostructure film after IR-light irradiation for 5 min (see Video I and the inset of Fig. 3A). However, upon visible light irradiation, the H_2 evolution amounts over the plasmonic film are much lower than the corresponding values obtained from IR-light irradiation (Fig. S3), which can be attributed to no coupling effect between Ag and $W_{18}O_{49}$ due to the mis-matched plasmonic absorption between Ag and $W_{18}O_{49}$ in visible light region. These observations imply that IR-driven strong plasmonic coupling between Ag NRs and $W_{18}O_{49}$ NWs occurs on their heterostructures film, which may not only boost the generation of plasmonic “hot electrons”, but also promote the localized temperature, thus leading to the photo/thermal synergistic enhancement of catalytic H_2 evolution from NH_3BH_3 aqueous solution.

To clarify the influence of the SPR-coupling-induced photothermal effect on the H_2 release from NH_3BH_3 , the reaction temperatures during the catalytic processes were measured over the different films upon IR-light excitation. As shown in the inset of Fig. 3A, the temperature is only 24°C (similar to room temperature) for the IR-irradiated reaction solution in the absence of a photocatalyst. However, after introducing the Ag/ $W_{18}O_{49}$ heterostructure film into the reaction solution, the reaction temperature could reach 55°C after only 5-min irradiation. This catalytic temperature is ~1.22 and ~1.96 times higher than the corresponding values obtained from the pure $W_{18}O_{49}$ NWs (45°C) and Ag NRs films (28°C), respectively. Please note that the plasmonic absorption band of $W_{18}O_{49}$ NWs is across the whole IR spectrum while the Ag NRs could only resonantly absorb the photon energy with a wavelength range from 900 to 1400 nm (see Fig. 1H). Thus, the photothermal effect of the $W_{18}O_{49}$ NWs film should be stronger than that of the Ag NRs film in response to irradiation with wavelengths exceeding 750 nm. Moreover, the enhanced reaction temperature on the catalytic system of the Ag/ $W_{18}O_{49}$ heterostructures film suggests the existence of plasmonic coupling between the Ag NRs and $W_{18}O_{49}$ NWs to promote the photothermal effect. Furthermore, a thermal imaging technique was used to confirm the real temperatures on the as-fabricated plasmonic films at atmospheric condition upon 980-nm irradiation. It should be point out that the photon energy at 980 nm can drive SPR of both Ag NRs and $W_{18}O_{49}$ NWs. Consequently, this should result in a plasmonic coupling on the Ag/ $W_{18}O_{49}$ heterostructures film. During the investigation, thermal images were acquired when the temperature reached a stable value (one minute after switching on the laser). As shown in Fig. 3B, the SPR excitation of $W_{18}O_{49}$ NWs can increase rapidly the located temperature from 22°C to 70.1°C, while the maximum temperature on the Ag NRs film is only 30.1°C. Interestingly, the located temperature of the Ag/ $W_{18}O_{49}$ heterostructures film (98.8°C) is obviously higher than that

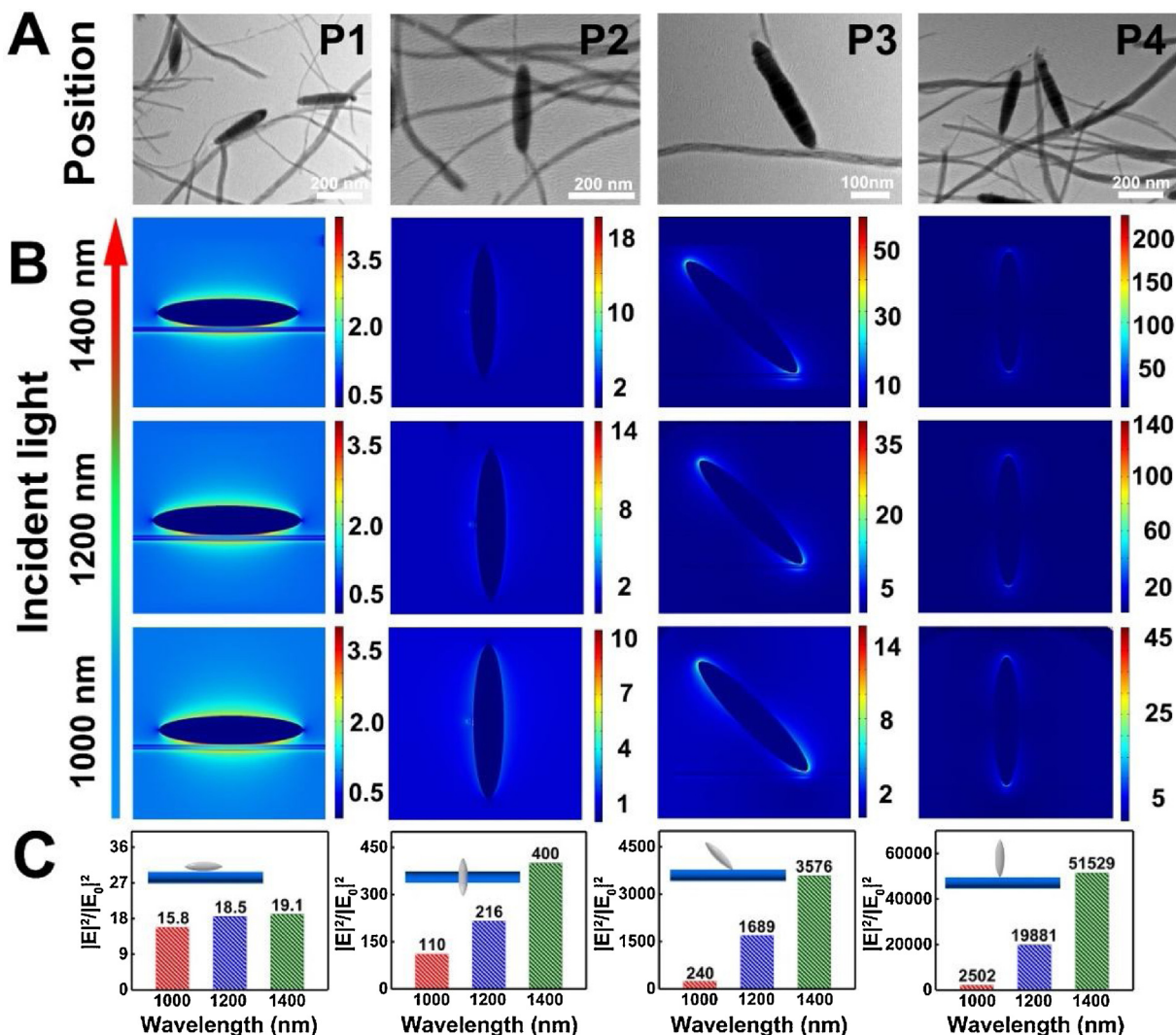


Fig. 2. (A) TEM images of various contact types between Ag NRs and W₁₈O₄₉ NWs in Ag/W₁₈O₄₉ heterostructures; (B) simulation results of electric field distributions at different contact-positions between Ag NR and W₁₈O₄₉ NWs with excitation wavelengths of 1000 nm, 1200 nm, and 1400 nm; (C) Simulated enhancements of electric-field intensities at plasmonic "hot spots" in Ag/W₁₈O₄₉ heterostructures as a function of different excited wavelengths; Insets show the corresponding binary heterostructures models of the contact positions between Ag NR and W₁₈O₄₉ NWs.

of the pure W₁₈O₄₉ NWs film (70.1°C), even though the existence of Ag NRs component that possesses a relative poor photothermal effect as compared to that of W₁₈O₄₉ NWs. This directly demonstrates the existence of plasmonic-coupling-improved photothermal effect to effectively promote the catalytic H₂ evolution over the Ag/W₁₈O₄₉ heterostructure film.

In addition to the photothermal effect, the plasmonic "hot electrons" also contribute to the enhancement of catalytic activity for H₂ evolution over the Ag/W₁₈O₄₉ heterostructure film upon SPR-coupling excitation by IR light. To verify this hypothesis, the reaction solution temperature was fixed at 15°C and the catalytic activities of the as-fabricated plasmonic films were retested under IR-light irradiation. The results indicated that after the weakening of the thermal effect, there was no H₂ evolution from NH₃BH₃ in the absence of photocatalysts (Fig. 3C). Notably, the Ag/W₁₈O₄₉ heterostructures film (~0.048 μmol min⁻¹) still exhibited the optimal photocatalytic activity for H₂ evolution with a rate exceeding those of the Ag NRs (~0.009 μmol min⁻¹) and W₁₈O₄₉ NWs films (~0.008 μmol min⁻¹) by ~5.3 fold and ~6.0 fold, respectively. These enhancement factors are a little lower than the corresponding values obtained from the IR-excited catalytic reaction without temperature control (~9.0 ×). These results indicate that plasmonic-coupling-excited "hot-electrons" take the leading role in the

enhanced catalytic activity of the Ag/W₁₈O₄₉ heterostructures film for H₂ evolution. Further investigation with this catalytic reaction condition showed that the apparent quantum efficiency (AQE) of the Ag/W₁₈O₄₉ heterostructures film could reach ~4.03% at 1250 nm, which is about four times higher than the AQE value of the pure Ag NRs (~1.06%) or W₁₈O₄₉ NWs (~1.01%) films (Fig. 3D). The AQE of ~4.03% is comparable to the corresponding values reported for common visible-light-driven semiconductor systems [49].

To further verify the IR-induced "hot electron" generation from as-fabricated plasmonic films, incident-photon-to-current-conversion efficiency (IPCE) measurements were conducted under irradiation at wavelengths ranging from 900 to 1500 nm. The standard equation of IPCE can be expressed as [50]:

$$\text{IPCE} = \frac{1240I}{\lambda J_{\text{light}}} \times 100\%$$

Where λ represents the incident light wavelength; J_{light} represents the incident light power density, and I is the photocurrent density. The obtained IPCE curves are presented in Fig. 3E, which shows that all the plasmonic films have the photo-responsive signals at the IR-light region. Moreover, the IPCE curve profiles basically correlate with their plasmonic absorption bands, which confirms the generation of "hot

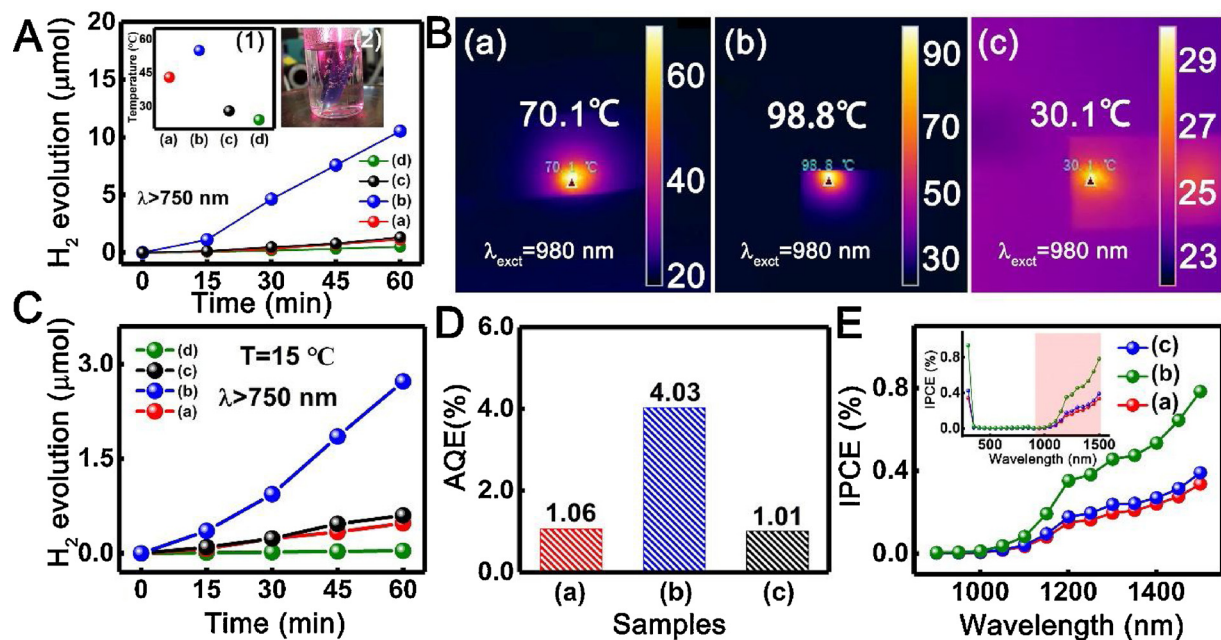


Fig. 3. (A) Plots of the H₂-evolution amount versus the reaction time of different catalysts in the NH₃BH₃ aqueous solution upon IR-light irradiation: (a) W₁₈O₄₉ NWs; (b) Ag/W₁₈O₄₉ heterostructures; (c) Ag NRs and (d) without any catalyst; inset (1) and (2) show the catalytic reaction temperature of different samples and the optical image of the reaction process, respectively; (B) thermal imaging of (a) W₁₈O₄₉ NWs, (b) Ag/W₁₈O₄₉ heterostructures and (c) Ag NRs under laser excitation at 980 nm; all images were obtained after the temperature reached steady values. (C) Time-dependent H₂-evolution from NH₃BH₃ aqueous solution at 15°C over different samples upon IR-light irradiation (a) W₁₈O₄₉ NWs; (b) Ag/W₁₈O₄₉ heterostructures; (c) Ag NRs and (d) without catalyst. (D) Apparent quantum efficiencies of different samples (a) W₁₈O₄₉ NWs; (b) Ag/W₁₈O₄₉ heterostructures, and (c) Ag NRs; (E) measured IPCE spectra of the as-fabricated films recorded at the incident wavelength range from 900 to 1500 nm at a potential of -0.2 V vs. Ag/AgCl in an aqueous solution of 0.02 M HCl: (a) W₁₈O₄₉ NWs, (b) Ag/W₁₈O₄₉ heterostructures, and (c) Ag NRs; inset: measured IPCE spectra recorded at the incident wavelength range from 300 to 1500 nm.

electrons" from the plasmon films due to the SPR excitation by IR light. Among these films, Ag/W₁₈O₄₉ heterostructures film displays the highest IPCE signal across the whole testing wavelength range. The IPCE value is about twice as large as that of either Ag NRs or W₁₈O₄₉ NWs films. This phenomenon can be attributed to two factors related to the kinetics process of plasmonic "hot electrons" [51]: (1) the SPR-coupling-improved generation process of "hot electrons" at the "hot spots" of Ag/W₁₈O₄₉ heterostructures (this has been proven via FEM simulation); (2) the suppressive relaxation of plasmonic "hot electrons" through an ultrafast electron transfer between Ag NRs and W₁₈O₄₉ NWs at their hetero-interface.

To investigate the second factor, transient absorption (TA) spectroscopy measurements were conducted of the as-fabricated samples. An excitation wavelength of 400 nm was selected to drive both the interband transition of W₁₈O₄₉ NWs and the Ag NRs' L-SPR. This detection can indicate whether the electron-transport channel is built in at the Ag/W₁₈O₄₉ heterostructures. As shown in Fig. 4A, the W₁₈O₄₉ NWs possesses a strong TA signal at the indicated wavelengths from 450 to 510 nm. Furthermore, a narrow TA band centered at 435 nm was found in the spectrum of Ag NRs. After coupling W₁₈O₄₉ NWs with Ag NRs to form the heterostructures, the feature signals of both the hetero-components could be observed. However, the TA signal of W₁₈O₄₉ NWs is greatly weakened in the spectrum of Ag/W₁₈O₄₉ heterostructures. Moreover, the Ag NRs in the heterostructures shows a blue-shifted absorption band compared to the corresponding result of pure Ag NRs. These results indicate the existence of photoinduced charge-transfer between Ag NRs and W₁₈O₄₉ NWs in their heterostructures. To further clarify the underlying kinetics process, the probe wavelength was fixed at 480 nm to compare the TA curves of W₁₈O₄₉ NWs and Ag/W₁₈O₄₉ heterostructures. As shown in Fig. 4B, the kinetics curve of W₁₈O₄₉ NWs obeys the biexponential function model [3]:

$$y = A_1 \cdot \exp(-t/\tau_1) + A_2 \cdot \exp(-t/\tau_2) + y_0$$

The obtained longer time constant (τ_1) of 11.6 ps can be ascribed to

the relaxation process of photoinduced electrons from the excited states (the energy levels in the conduction band of W₁₈O₄₉) to the ground state (the valence band of W₁₈O₄₉). The shorter time constant (τ_2) of 1.3 ps is related to the electron trapping process via defect states of W₁₈O₄₉. However, in the case of Ag/W₁₈O₄₉ heterostructures, the TA kinetics curve at 480 nm (Fig. 4C) follows a monoexponential function [3]:

$$y = A \cdot \exp(-t/\tau) + y_0$$

The fitted result indicates the existence of one decay process of the photoinduced electron from the W₁₈O₄₉ hetero-component with the time constant (τ) of 2.6 ps. This value is a little longer than the time (τ_1) for the fast decay process of W₁₈O₄₉; however, it is much shorter than that of the slow decay process. Thus, it is reasonable to deduce that the transport channel of photoinduced electrons is formed at the Ag/W₁₈O₄₉ interface, leading to a fast electron transfer from the W₁₈O₄₉ to Ag hetero-components with a time constant shorter than 2.6 ps. This electron transfer in the heterostructure increased the electron density of plasmonic hetero-components of Ag NRs. In theory, the plasmon resonance wavelength of metal nanostructures depends on the electron density, which is expressed by the following function [24]:

$$\lambda = \left[\frac{4\pi^2 c^2 m_e \epsilon_0}{Ne^2} \right]^{1/2}$$

Where λ represents the plasmonic resonance wavelength; Ne represents the electron density of metal nanostructures; m_e represents the effective mass. It can be concluded that the blue-shift of the L-SPR band of Ag NRs in the heterostructures is attributed to the increased electron density due to the interfacial electron transfer from W₁₈O₄₉ to Ag hetero-components, as illustrated in Fig. 4D and S4(A and B).

The formed high-quality channel for the charge transfer would also accelerate the separation of IR-excited plasmonic "hot electrons" in the Ag/W₁₈O₄₉ heterostructures. To confirm this point, an IR-excited

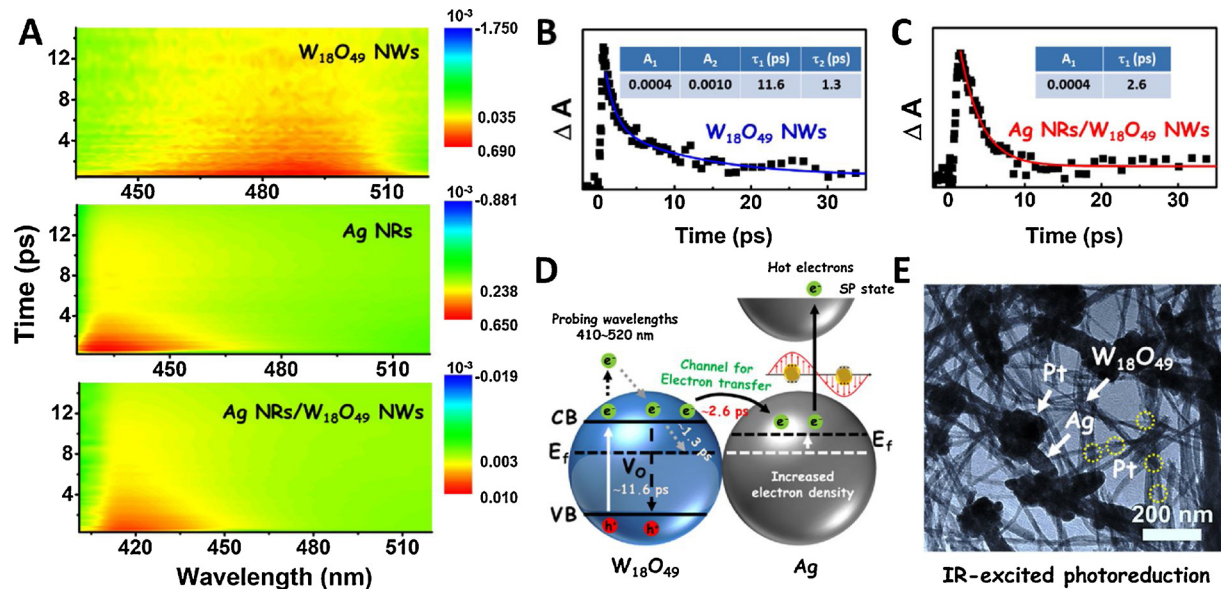
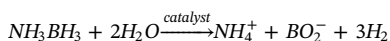


Fig. 4. (A) Ultrafast TA spectra of $W_{18}O_{49}$ NWs, Ag NRs, and $Ag/W_{18}O_{49}$ heterostructures; TA kinetics curves of (B) $W_{18}O_{49}$ NWs and (C) $Ag/W_{18}O_{49}$ heterostructures with a probing wavelength at 480 nm; (D) schematic of the kinetics process of the interfacial electron transfer in the $Ag/W_{18}O_{49}$ heterostructures; (E) TEM image of the Pt nanoparticles-loaded $Ag/W_{18}O_{49}$ heterostructures fabricated via IR-excited photoreduction reaction.

photoreduction reaction was conducted on the $Ag/W_{18}O_{49}$ heterostructures in the presence of Pt^{4+} ions. Upon the SPR-coupling excitation by IR-light, the Pt nanoparticles can be loaded on the surface of the heterostructures via photoreduction of Pt^{4+} ions into Pt° by the plasmonic “hot electrons” (Fig. S4C). As shown in Fig. 4E, a large number of Pt nanoparticles are positioned at the tips of Ag NRs, in particular, these are positioned at the strong coupling areas of such plasmonic “hot spots” at the interface between the tips of Ag NRs and the $W_{18}O_{49}$ NWs. These observations indicate that the relaxation process of IR-excited plasmonic “hot electrons” can be powerfully hindered through the interfacial charge transfer from Ag to $W_{18}O_{49}$ in the heterostructures. Moreover, the Ag NRs as the “electron sink” also provides abundant active sites for IR-excited catalytic H_2 evolution from the NH_3BH_3 .

The underlying mechanism of the enhanced catalytic H_2 evolution for plasmonic-coupling effect on $Ag/W_{18}O_{49}$ heterostructures film is illustrated in Scheme 1. The catalytic hydrolysis of NH_3BH_3 for H_2 evolution over the suitable catalysts is according to the following Equation [52–55]:



In general, the catalyst will absorb NH_3BH_3 molecules together with H_2O to make them activation for the hydrolysis reaction (Scheme 1) [55]. In our case, the plasmonic-coupling excitation of $Ag/W_{18}O_{49}$ heterostructures by IR light would induce an intense localized electric field, thereby leading to the generation of abundant plasmonic “hot electrons” at the interface of $Ag/W_{18}O_{49}$. Owing to the “hot electron” transfer from $W_{18}O_{49}$ to Ag in their heterostructure, the Ag should be a relatively negative hetero-component as compare to the hydride-acceptor of $W_{18}O_{49}$ hetero-component [56]. In this way, the accumulated “hot electrons” on the Ag surface can facilitate the absorption of NH_3BH_3 and H_2O molecules, and then further transfer to NH_3BH_3 , forming the negative charged -H in -BH₃ group. These negative charged -H is more easier to reactive the activated H_2O molecule for boosting the H_2 evolution (scheme1(2)) [56,57]. Meanwhile, the hydride-acceptor of $W_{18}O_{49}$ can also react with adsorbed H_2O molecules to generate hydroxyl radicals (·OH) [56]. The hydroxyl radicals (·OH) would interact with NH_3BH_3 to form the activated transition state complexes [58,59]. In addition to the plasmon-induced hot electrons, the photo-thermal effect also contributes to the enhancement of catalytic activity for H_2 evolution on the $Ag/W_{18}O_{49}$ heterostructures by hydrolyzing

NH_3BH_3 under IR irradiation (scheme1(3)). The localized temperature upon SPR-coupling excitation can overcome a small energy barrier in the hydrolysis reaction, so as to accelerate the H_2 evolution reaction [60]. Moreover, the localized temperature may also speed up the H_2 -desorption process on the surface of $Ag/W_{18}O_{49}$ heterostructures, thereby boosting the catalytic reaction for H_2 evolution.

Furthermore the influence of the coverage density of Ag NRs on the IR-excited catalytic activity of the $Ag/W_{18}O_{49}$ heterostructures film for H_2 evolution was studied. The SEM images and UV-vis-IR absorption spectra results (Figs. S5 and S6) indicate that the plasmonic coupling intensity of the $Ag/W_{18}O_{49}$ heterostructures film develops relative to the coverage density of Ag-NRs component. When $W_{18}O_{49}$ NWs are fully covered by the Ag NRs in the heterostructures film, the intensity of the SPR-coupling band decreases noticeably and its profile is similar to the L-SPR band of pure Ag NRs. This is because the “mirror effect” of compact Ag layer reflects the incident light and thus reduces the plasmonic coupling interaction. In this way, the IR-excited catalytic activity of the plasmonic heterostructure film increases with the coverage density of Ag NRs. However, when the surface of the heterostructures film is fully occupied by the Ag NRs, the catalytic activity starts to decrease (Fig. S7).

The stability of the $Ag/W_{18}O_{49}$ heterostructure film was assessed by executing a cycling test of IR-irradiated catalytic H_2 evolution without controlling the reaction temperature (Fig. 5A). The recycled heterostructure film can retain the activity for H_2 evolution well with negligible deactivation after three cycles. The catalytic stability of $Ag/W_{18}O_{49}$ heterostructures film is better than that of other nonmetallic plasmonic nanostructures [3,35,61]. This is because that the hot electron used for catalytic H_2 evolution can be further repaid to the plasmonic heterostructures film through the hydroxyl oxygen in water due to the existence of electron-acceptor Ag, as illustrated in Scheme 1. The photon energy in IR region accounts for nearly a half of the incoming solar energy (~44%). Therefore, focused sunlight was used to drive the catalytic activity for H_2 evolution from NH_3BH_3 over the $Ag/W_{18}O_{49}$ heterostructure film (Fig. 5B). Surprisingly, after irradiation by this focused sunlight for 1 h, the H_2 evolution of the heterostructures film could reach ~2.76 μ mol, accompanied with a conspicuous H_2 -bubble production (see video II). Overall, it is reasonable to assume that the IR-induced plasmon-coupling effect in the noble metal/semiconductor nanostructural plasmonic photocatalyst can significantly increase both

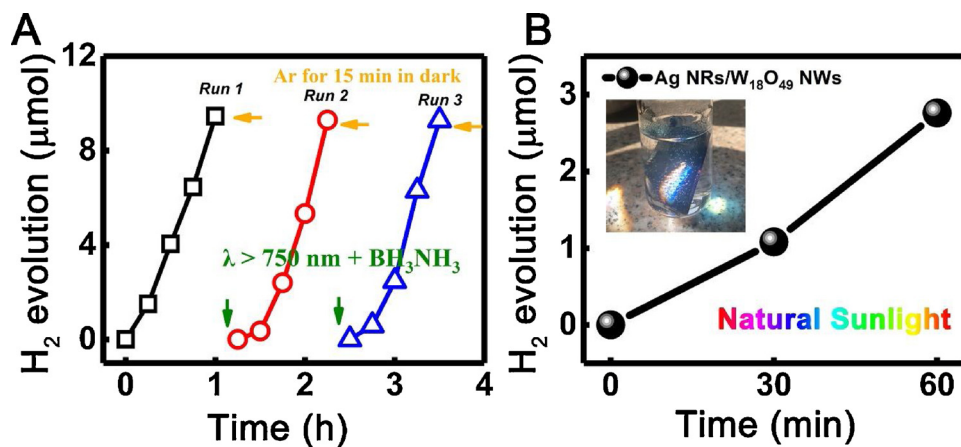


Fig. 5. (A) Cycling test of the catalytic H₂ evolution from NH₃BH₃ aqueous solution over the Ag/W₁₈O₄₉ heterostructures film under IR-light irradiation; (B) Catalytic H₂ evolution of the as-fabricated Ag/W₁₈O₄₉ heterostructures film upon focused sunlight irradiation.

the generation and separation of “hot electrons” and the photothermal effect, thus synergistically enhancing the catalytic activity for H₂ evolution from NH₃BH₃.

4. Conclusions

In summary, the IR-driven strong plasmonic coupling phenomenon has been demonstrated in a novel type of metal/non-metal heterostructures system fabricated through assembling Ag NRs onto the W₁₈O₄₉ NWs film. The resonance excitation of both W₁₈O₄₉ NWs and Ag NRs in their heterostructures can greatly magnify the localized electric field of incident light from 10¹ to 10⁴ times depending on the contact modes of the hetero-interface. This process not only improves the generation and separation of plasmonic “hot electrons”, but also increases the localized temperature at the IR-excited plasmonic “hot spots” of the Ag/W₁₈O₄₉ heterostructures film. Thus, upon focused sunlight irradiation, the photo/thermal synergistic catalytic ammonia borane into H₂ was observed over the Ag/W₁₈O₄₉ heterostructure film. The H₂ evolution rate reached ~2.76 μmol h⁻¹. This type of metal/non-metal heterostructure system also offers an enormous potential for the application in photoelectronic devices with ultra-broad photoresponse region.

Acknowledgements

This work is supported by the National Natural Science Foundation of China (Grant Nos: 51772041, 11474046, 61775024, 11704058, and 21503034), the Natural Science Foundation of Liaoning Province (Grant Nos: 20170540190), the Program for Liaoning Excellent Talents in University (LNET) (Grant Nos. LR2015016 and LR2017004), the Program for Dalian Excellent Talents (Grant No. 2016RQ069), the Science and Technique Foundation of Dalian (Grant Nos. 2014J11JH134 and 2015J12JH201), and the Foundation (Grant No. DUT16RC(3)111). Zhenyi Zhang thanks the supports from the “Dalian Science Foundation for Distinguished Young Scholars (2018)” and the “LiaoNing Revitalization Talents Program (XLYC1807176)”.

Appendix A. Supplementary data

Supplementary material related to this article can be found, in the online version, at doi:<https://doi.org/10.1016/j.apcatb.2019.04.035>.

References

- [1] C.M. Wolff, P.D. Frischmann, M. Schulze, B.J. Bohn, R. Wein, P. Livadas, M.T. Carlson, F. Jäckel, J. Feldmann, F. Würthner, J.K. Stolarczyk, *Nat. Energy* 3 (2018) 862–869.
- [2] K. Iwashina, A. Iwase, Y.H. Ng, R. Amal, A. Kudo, *J. Am. Chem. Soc.* 137 (2015) 604–607.
- [3] Z. Zhang, X. Jiang, B. Liu, L. Guo, N. Lu, L. Wang, J. Huang, K. Liu, B. Dong, *Adv. Mater.* 30 (2018) 1705221.
- [4] F. Qiu, Z. Han, J.J. Peterson, M.Y. Odoi, K.L. Sowers, T.D. Krauss, *Nano Lett.* 16 (2016) 5347–5352.
- [5] Y. Ren, Q. Xu, X. Zheng, Y. Fu, Z. Wang, H. Chen, Y. Weng, Y. Zhou, *Appl. Catal. B-Environ.* 231 (2018) 381–390.
- [6] P. Verma, K. Yuan, Y. Kuwahara, K. Mori, H. Yamashita, *Appl. Catal. B-Environ.* 223 (2017) 10–15.
- [7] D. Özhaba, N.Z. Kılıçaslan, S. Özkar, *Appl. Catal. B-Environ.* 162 (2015) 573–582.
- [8] J. Song, X. Gu, J. Cheng, N. Fan, H. Zhang, H. Su, *Appl. Catal. B-Environ.* 225 (2018) 424–432.
- [9] H. Wang, L. Zhang, Z. Chen, J. Hu, S. Li, Z. Wang, J. Liu, X. Wang, *Chem. Soc. Rev.* 45 (2015) 5234–5244.
- [10] Z. Bian, T. Tachikawa, P. Zhang, M. Fujitsuka, T. Majima, *J. Am. Chem. Soc.* 136 (2014) 458–465.
- [11] S. Linic, P. Christopher, D.B. Ingram, *Nat. Mater.* 10 (2011) 911–921.
- [12] K. Wu, J. Chen, J.R. McBride, T. Lian, *Science* 349 (2015) 632–635.
- [13] A. Vaneski, A.S. Susha, J. Rodríguez-Fernández, M. Berr, F. Jäckel, J. Feldmann, A.L. Rogach, *Adv. Funct. Mater.* 21 (2011) 1547–1556.
- [14] R. Jiang, B. Li, C. Fang, J. Wang, *Adv. Mater.* 26 (2015) 5274–5309.
- [15] M. Wang, M. Ye, J. Iocozzia, C. Lin, Z. Lin, *Adv. Sci.* 3 (2016) 1600024.
- [16] L. Zhou, D.F. Sweare, C. Zhang, H. Robatjazi, H. Zhao, L. Henderson, L. Dong, P. Christopher, E.A. Carter, P. Nordlander, *Science* 362 (2018) 69–72.
- [17] Z. Lou, M. Fujitsuka, T. Majima, *J. Phys. Chem. Lett.* 8 (2017) 844–849.
- [18] Z. Lou, M. Fujitsuka, T. Majima, *ACS Nano* 10 (2016) 6299–6305.
- [19] Z. Lou, Z. Wang, B. Huang, Y. Dai, *Chemcatchem* 6 (2015) 2456–2476.
- [20] A.K.F. Bilge Coşkuner Filiz, Sabriye Pişkin, *Appl. Catal. B-Environ.* 238 (2018) 365–380.
- [21] J. Zhang, W. Chen, H. Ge, C. Chen, W. Yan, G. Zhe, G. Jie, B. Zhang, X. Duan, Q. Yong, *Appl. Catal. B-Environ.* 235 (2018) 256–263.
- [22] X. Zhou, G. Liu, J. Yu, W. Fan, J. Mater. Chem. 22 (2012) 21337–21354.
- [23] U. Aslam, V.G. Rao, S. Chavez, S. Linic, *Nat. Catal.* 1 (2018) 656–665.
- [24] P.K. Jain, M.A. El-Sayed, *Chem. Phys. Lett.* 487 (2015) 153–164.
- [25] J. Wu, Z. Zhang, B. Liu, Y. Fang, L. Wang, B. Dong, *Sol. Rrl* 2 (2018) 1800039.
- [26] N. Li, X. Cao, Y. Li, T. Chang, S. Long, Y. Zhou, G. Sun, L. Ge, P. Jin, *Chem. Commun. (Camb.)* 54 (2018) 5241–5244.
- [27] L. Xin, S. Mark T, *Chem. Soc. Rev.* 43 (2014) 3908–3920.
- [28] Z. Shu, P. Xiaodong, N. Zhenyi, D. Yi, J. Yingying, J. Chuanhong, D. Christophe, Y. Deren, N. Tomohiro, *ACS Nano* 9 (2014) 378–386.
- [29] J.M. Luther, P.K. Jain, E. Trevor, A.A. Paul, *Nat. Mater.* 10 (2011) 361–366.
- [30] D. Dirk, H.R. Thomas, M. Karol, N.C. Bigall, K. Mee Rahn, G. Alessandro, F. Andrea, P. Mauro, M. Liberato, *J. Am. Chem. Soc.* 133 (2011) 11175–11180.
- [31] K. Masayuki, K. Hayato, Y. Taizo, T. Toshiharu, *J. Am. Chem. Soc.* 131 (2009) 17736–17737.
- [32] S.H. Lee, H. Nishi, T. Tatsuma, *Nanoscale* 10 (2018) 2841–2847.
- [33] D. Zhou, D. Liu, W. Xu, Z. Yin, X. Chen, P. Zhou, S. Cui, Z. Chen, H. Song, *ACS Nano* 10 (2016) 5169–5179.
- [34] A.M. Schimpf, S.D. Lounis, E.L. Runnerstrom, D.J. Milliron, D.R. Gamelin, *J. Am. Chem. Soc.* 137 (2015) 518–524.
- [35] Z. Lou, Q. Gu, L. Xu, Y. Liao, C. Xue, *Chem. Asian J.* 10 (2015) 1291–1294.
- [36] C. Hefeng, K. Takashi, M. Kohsuke, Y. Hiromi, *Angew. Chem. Int. Ed.* 53 (2014) 2910–2914.
- [37] L. Jianhua, H. Jianguo, K. Zhichen, G. Reza, X. Nannan, L. Hongpeng, H. Xueli, *Nanoscale* 6 (2014) 5770–5776.
- [38] L. Bo, Z. Yuxin, Z. Ruija, W. Qian, Z. Bingjie, A. Lei, Y. Fei, H. Yingqi, H. Junqing, *Dalton Transactions* 43 (2014) 6244–6250.
- [39] J.-J. Li, E.-Q. Yu, S.-C. Cai, X. Chen, J. Chen, H.-P. Jia, Y.-J. Xu, *Appl. Catal. B-Environ.* 240 (2019) 141–152.
- [40] J.H. Lee, J.Y. Do, N.-K. Park, M.W. Seo, H.-J. Ryu, J.-P. Hong, Y.S. Kim, S.K. Kim,

M. Kang, J. Photochem. Photobiol. A: Chem. 364 (2018) 219–232.

[41] J. Li, Y. Ye, L. Ye, F.-Y. Su, Z. Ma, J. Huang, H. Xie, D.E. Doronkin, A. Zimina, J.-D. Grunwaldt, J. Mater. Chem. A Mater. Energy Sustain. (2019).

[42] L. Wang, Y. Wang, Y. Cheng, Z. Liu, Q. Guo, M.N. Ha, Z. Zhao, J. Mater. Chem. A Mater. Energy Sustain. 4 (2016) 5314–5322.

[43] E.T. Kho, T.H. Tan, E. Lovell, R.J. Wong, J. Scott, R. Amal, Green Energy Environ. 2 (2017) 204–217.

[44] T.H. Tan, J. Scott, Y.H. Ng, R.A. Taylor, K.-F. Aguey-Zinsou, R. Amal, ACS Catal. 6 (2016) 1870–1879.

[45] B. Dong, D. Qin, H.L. Shi, Y.R. Fang, W.Z. Wang, Y.Y. He, B.S. Cao, Y.X. Liu, Y. Ding, Microchim. Acta. 181 (2014) 791–795.

[46] H. Wei, A. Reyes-Coronado, P. Nordlander, J. Aizpurua, H. Xu, ACS Nano 4 (2010) 2649–2654.

[47] V.G. Kravets, A.V. Kabashin, W.L. Barnes, A.N. Grigorenko, Chem. Rev. 118 (2018) 5912–5951.

[48] Z. Zhang, J. Huang, Y. Fang, M. Zhang, K. Liu, B. Dong, Adv. Mater. 29 (2017) 1606688.

[49] Z. Zhang, Y. Huang, K. Liu, L. Guo, Q. Yuan, B. Dong, Adv. Mater. 27 (2015) 5906–5914.

[50] Z. Zhang, K. Liu, Y. Bao, B. Dong, Appl. Catal. B-Environ. 203 (2017) 599–606.

[51] Y. Zhang, S. He, W. Guo, Y. Hu, J. Huang, J.R. Mulcahy, W.D. Wei, Chem. Rev. 118 (2017) 2927–2954.

[52] S. Akbayrak, Y. Tonbul, S. Özkar, Appl. Catal. B-Environ. 198 (2016) 162–170.

[53] A. Bulut, M. Yurderi, I.E. Ertas, M. Celebi, M. Kaya, M. Zahmakiran, Appl. Catal. B-Environ. 180 (2016) 121–129.

[54] S. Akbayrak, P. Erdek, S. Özkar, Appl. Catal. B-Environ. 142-143 (2013) 187–195.

[55] K. Feng, J. Zhong, B. Zhao, H. Zhang, L. Xu, X. Sun, S.T. Lee, Angew. Chem. Int. Ed. 55 (2016) 11950–11954.

[56] Y. Lou, J. He, G. Liu, S. Qi, L. Cheng, J. Chen, Y. Zhao, J.J. Zhu, Chem. Commun. 54 (2018) 6188–6191.

[57] Z. Li, T. He, L. Liu, W. Chen, M. Zhang, G. Wu, P. Chen, Z. Li, T. He, L. Liu, Chem. Sci. 8 (2016) 781.

[58] H. Yin, Y. Kuwahara, K. Mori, H. Cheng, M. Wen, H. Yamashita, J. Mater. Chem. A 5 (2017) 8946–8953.

[59] C.-C. Hou, Q. Li, C.-J. Wang, C.-Y. Peng, Q.-Q. Chen, H.-F. Ye, W.-F. Fu, C.-M. Che, N. López, Y. Chen, Energy Environ. Sci. 10 (2017) 1770–1776.

[60] O. Komova, V. Simagina, N. Kayl, G. Odegova, O. Netskina, Y. Chesalov, A. Ozerova, Int. J. Hydrogen Energy 38 (2013) 6442–6449.

[61] Z. Zhang, Y. Liu, Y. Fang, B. Cao, J. Huang, K. Liu, B. Dong, Adv. Sci. 5 (2018) 1800748.